ChemElectroChem

Chemistry Europe
European Chemical Societies Publishing

ChemElectroChem

RESEARCH ARTICLE OPEN ACCESS

Pressure-Dependent Electronic and Ionic Tortuosities During Fabrication of Composite Cathodes for All-Solid-State Batteries: Influence of Active Material Particle Morphology, Volume Fraction, and Coating

Vanessa Miß[1] | Greta Müller[1] | Sophie Schäfer[1] | Evelyn Versok[1] | Stefan Seus[1] | Valeriu Mereacre[2] | Joachim R. Binder[2] | Bernhard Roling[1]

[1]Department of Chemistry and Marburg Center for Quantum Materials and Sustainable Technologies (mar.quest), University of Marburg, Marburg, Germany | [2]Karlsruhe Institute of Technology (KIT), Institute for Applied Materials (IAM-ESS), Eggenstein-Leopoldshafen, Karlsruhe, Germany

Correspondence: Bernhard Roling (roling@staff.uni-marburg.de)

Received: 16 February 2026 | **Revised:** 8 June 2026 | **Accepted:** 26 June 2026

Keywords: composite cathode | impedance spectroscopy | ionic and electronic tortuosity | $LiNbO_3$ coating | pressure dependence | single-crystalline and polycrystalline NMC622

ABSTRACT

The cathode of bulk-type all-solid-state batteries (ASSBs) is a composite consisting of cathode active material (CAM) particles and solid electrolyte (SE) particles. Since ASSBs are usually fabricated and cycled under pressure, it is important to achieve a better understanding of the influence of pressure on the electronic and ionic transport in CAM/SE composites. However, experimental values for pressure-dependent electronic and ionic conductivities of CAM/SE composites are scarce. Therefore, we have carried out pressure-dependent impedance spectroscopic measurements during compaction of composite powders under an increasing fabrication pressure up to 663 MPa. The composites contained four different types of $LiNi_{0.6}Mn_{0.2}Co_{0.2}O_2$ (NMC622) cathode active material particles: (i) single-crystalline and uncoated, (ii) single-crystalline and coated with $LiNbO_3$, (iii) polycrystalline and uncoated, and (iv) polycrystalline and coated with $LiNbO_3$. In addition, the volume fractions of CAM particles and SE particles were varied. The physical meaning of the resistances extracted from the impedance spectra were analyzed, and electronic and ionic tortuosities were calculated. A strong influence of the CAM particle morphology and coating on the microstructure of the composites was observed. Based on the results, the interrelation between composite microstructure and tortuosities is discussed.

1 | Introduction

Lithium-ion batteries are increasingly used in electric vehicles and for renewable energy storage. For these fields of application, improvements in gravimetric and volumetric energy density as well as in battery safety are important issues [1–4]. Such improvements should be achievable by the further development of all-solid-state batteries (ASSBs): (i) Replacing the flammable carbonate-based electrolyte in conventional Li-ion batteries by a non-flammable solid electrolyte (SE) in ASSBs reduces the risk of a battery fire [5–8], and (ii) if a lithium metal anode can be successfully cycled in ASSBs without dendrite formation, the volumetric energy density can be enhanced by about 70% [1].

Despite these potential advantages of ASSBs, a major challenge is the establishment of fast electron and ion transport pathways in the battery, in particular inside the composite cathode consisting of cathode active material (CAM) particles and solid electrolyte

(SE) particles [9]. An inhomogeneous distribution of CAM and SE particles, the coating of CAM particles with thin ion-conducting layers as well as gaps between the particles can slow down ion and electron transport [10].

The hindrance of electron transport in a composite electrode as compared to the pure CAM can be described by the electronic tortuosity τ_{eon}. The electronic resistance of a composite electrode is then defined as: $R_{eon} = \frac{1}{\sigma_{eon}^{CAM}} \cdot \frac{\tau_{eon}}{\varepsilon_{CAM}} \cdot \frac{d}{A}$. Here, σ_{eon}^{CAM} and ε_{CAM} denote the electronic conductivity of the pure CAM and the volume fraction of the CAM in the composite, respectively, while d and A are the thickness and the area of the electrode. The same type of relation can be given for ion transport resistance of a composite electrode, $R_{ion} = \frac{1}{\sigma_{ion}^{SE}} \cdot \frac{\tau_{ion}}{\varepsilon_{SE}} \cdot \frac{d}{A}$ with the ionic tortuosity τ_{ion}. Here, σ_{ion}^{SE} and ε_{SE} denote the ionic conductivity of the pure SE and the volume fraction of the SE in the cathode, respectively. The electronic tortuosity τ_{eon} and the ionic tortuosity τ_{ion} are governed by the length of the respective transport pathways and by bottlenecks (constrictivites) along the pathways [11]. τ_{eon} and τ_{ion} are strongly influenced by the volume fractions of the solid electrolyte particles ε_{SE} and of the cathode active material particles ε_{CAM} [12, 13], by the size ratio of SE particles to CAM particles [12, 14, 15], as well as by the fabrication pressure of the cathode pellet [12, 13]. While ionic and electronic tortuosities have been determined at selected pressures, systematic studies on the pressure dependence of tortuosities in composite cathodes are scarce. Park et al. studied the pressure dependence of the ionic tortuosity τ_{ion} in a cell under electron-blocking conditions and found a drop of the tortuosity from values in the range of $\tau_{ion} = 20-75$ at 40 MPa to values in the range of $\tau_{ion} = 5-15$ at 660 MPa [16]. So et al. observed a similar drop of τ_{ion} with increasing pressure in discrete-element simulations of composite electrodes for ASSBs [17]. To the best of our knowledge, a study on the pressure dependence of the electron transport tortuosity τ_{eon} has not yet been published.

In this study, we have carried out pressure-dependent impedance spectroscopy on various composite electrodes for ASSBs in combination with SEM/EDX imaging of the electrodes. The impedance measurements were carried out in situ under an increasing fabrication pressure up to 663 MPa during the *first compaction* of the composite powder. The aim is to obtain a better understanding of the influence of irreversible processes taking place during compaction on the ionic and the electronic transport in the obtained electrode pellets. High fabrication pressures of several 100 MPa are also conceivable in the case of practical ASSBs. The pellets contain variable volume fractions of single-crystalline or polycrystalline $LiNi_{0.6}Mn_{0.2}Co_{0.2}O_2$ (NMC622) cathode active material particles and of amorphous 0.67 Li_3PS_4 + 0.33 LiI solid electrolyte particles. The CAM particles are either uncoated or coated with a thin amorphous $LiNbO_3$ layer. The obtained pressure-dependent impedance spectra are analyzed, and the physical meaning of the obtained resistances is discussed. Pressure-dependent tortuosities τ_{eon} and τ_{ion} are calculated, and the influence of the NMC622 particle morphology (single-crystalline vs. polycrystalline), volume fraction, and coating on the tortuosities is discussed. Thereby, we obtain deeper insights into the impedance spectra of fully lithiated composite cathodes, which should be helpful for the interpretation of the impedance spectra of partially or fully delithiated cathodes.

2 | Experimental Section

All sample preparations were carried out in a glovebox (UniLab, MBraun, Garching, Germany) under an argon atmosphere with $x_{H2O} < 1$ ppm and $x_{O2} < 1$ ppm.

A 2 g batch of the solid electrolyte 0.67 Li_3PS_4 + 0.33 LiI was synthesized in a planetary ball mill (Pulverisette 7 premium line, Fritsch, Idar-Oberstein, Germany) by mixing Li_2S (99,9%, Alfa Aesar, Karlsruhe, Germany), P_2S_5 (for synthesis, Sigma Aldrich, Taufkirchen, Germany) and LiI (99,999%, Alfa Aesar, Karlsruhe, Germany) powder in stoichiometric ratio in a 20 mL zirconia pot with 10 zirconia balls (diameter 10 mm). Then, the pot was closed air-tight, removed from the glovebox, and integrated into the ball mill. The milling time was about 8 h (99 cycles; 5 min milling; 15 min rest) with a rotation speed of 700 rpm. After milling, the pot was opened inside the glovebox, and the electrolyte was grinded in an agate mortar to obtain the product powder. The powder was filled into a mark tube (Hilgenberg, Marsfeld, Germany) under argon, and the mark tube was closed air-tight using a wax. XRD measurements using a powder diffractometer STOE STADI MP (STOE, Darmstadt, Germany) with Cu Kα radiation in a Debye-Scherrer geometry confirmed the amorphous nature of the powder, see Figure S1.

$LiNi_{0.6}Mn_{0.2}Co_{0.2}O_2$ (NMC622) was purchased as uncoated polycrystalline particles and as uncoated single-crystalline particles, respectively, from MSE Supplies (Tucson, USA). A fraction of the NMC622 particles were coated by $LiNbO_3$ (0.5 wt%) using a chemically activated coating process with H_2O_2 as activating agent [18, 19]. As compared to a classical sol–gel coating process, the chemically activated process leads to denser coatings with a more homogeneous thickness. Finally, the coated particles were heat-treated at 350 °C leading to an amorphous structure of the coating [19].

The composite cathodes were prepared in an agate mortar by mixing different volume ratios of the CAM particles and the SE particles for 15 min. The CAM:SE volume ratios were 70:30, 50:50 and 30:70, respectively, in the case of the uncoated NMC622 particles and 60:40, 50:50 and 40:60, respectively, in the case of the coated NMC622 particles.

The impedance measurements were carried out using the electrochemical laboratory press CompreDrive (rhd instruments, Darmstadt, Germany) in an active force control mode. To this end, the respective composite cathode powder (weight 40 and 80 mg, respectively) was filled into the airtight sample cell (CompreCell, rhd instruments, Darmstadt, Germany), and a pressure was applied by using WC pistons acting also as electrodes. The starting pressure was 8.8 MPa. In a first step, the pressure was increased in 8.8 MPa steps up to 97 MPa. Then, the pressure was increased in 24.25 MPa steps to 194 MPa. Subsequently, the pressure was increased in 49 MPa steps to 292 MPa, followed by an increase up to 584 MPa in 97 MPa steps. Finally, the pressure was increased to 663 MPa (see pressure protocol in Figure S2). The same procedure was used for the impedance measurements on the pure solid electrolyte 0.67 Li_3PS_4 + 0.33 LiI. Impedance spectra at 25 °C and at the different pressures were taken by means of the

NEISYS Potentiostat/Galvanostat/EIS Base Unit (Novocontrol Technologies, Montabaur, Germany) in a frequency range from 1 MHz to 0.1 Hz with an applied AC voltage of 10 mV_{rms}. The impedance spectra were analyzed with the software RelaxIS (rhd instruments, Darmstadt, Germany).

SEM imaging of the cathode active materials powder, of the composite cathode powder and of pellets after finalizing the impedance measurements was carried out with a secondary electron microscope (Crossbeam 550, Zeiss, Oberkochen, Germany). To this end, the respective powder or pellet was fixed on a carbon-based sample holder inside the glovebox and was transferred to the SEM under inert gas conditions in a sample transfer shuttle (Semilab Conductor Physics Laboratory Co. Ltd., Budapest, Hungary). The SEM images were taken by applying a voltage of 5 kV and a current of 100 pA. In addition, energy-dispersive X-ray spectroscopy (EDX) was carried out at 5 kV and 1 or 2 nA using an Ultim Max detector (Oxford Instruments, Abington, United Kingdom).

3 | Results and Discussion

3.1 | Pressure-Dependent Ionic Conductivity of the Pure Solid Electrolyte Pellet

In Figure 1, the ionic conductivity of the pure 0.67 $Li_3PS_4 + 0.33$ LiI solid electrolyte pellet, σ_{ion}^{SE}, is plotted versus pressure p. σ_{ion}^{SE} increases from about 10^{-4} Scm^{-1} at low pressures to about 10^{-3} Scm^{-1} at high pressures. At high pressures, the ionic conductivity becomes virtually independent of the pressure.

3.2 | Pressure-Dependent Impedance Spectra of Composite Cathodes With Two Different Thicknesses

In Figure 2a, impedance spectra of two composite cathodes with a thickness of 128 and 246 µm, respectively, taken at a pressure of 486 MPa are shown. Both cathodes are composed of 50 vol% uncoated pc-NMC622 particles and 50 vol% 0.67 $Li_3PS_4 + 0.33$ LiI particles. The impedance spectra are characterized by a high-frequency resistance R_1 and by two semicircles. The diameters of these two semicircles are denoted by R_2 and R_3, respectively. In order to determine the values of the three resistances R_1, R_2, and R_3, the spectra were fitted by the equivalent circuit shown in the inset. In Figure 2b, we plot the high-frequency resistance R_1, the intermediate-frequency resistance $R_1 + R_2$, and the low-frequency resistance $R_1 + R_2 + R_3$ versus the thickness d of the composite cathodes. All resistances are proportional to the thickness of the cathode. This implies that all resistances are bulk resistances.

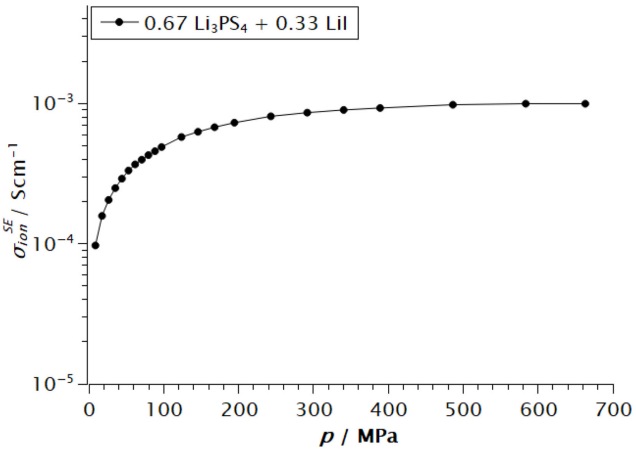

FIGURE 1 | Pressure-dependent ionic conductivity $\sigma_{ion}^{SE}(p)$ of a 0.67 $Li_3PS_4 + 0.33$ LiI solid electrolyte pellet.

3.3 | Pressure-Dependent Impedance Spectra of Composite Cathodes With Different Volume Fractions of Active Material and Solid Electrolyte

In Figure 3, Nyquist impedance plots are shown for a composite with 30 vol% uncoated pc-NMC622 particles and 70 vol% 0.67 $Li_3PS_4 + 0.33$ LiI particles as well as for a composite with 70 vol% uncoated pc-NMC622 particles and 30 vol% 0.67 $Li_3PS_4 + 0.33$ LiI particles. In the case of the composite with the low volume fraction of CAM particles, the low-frequency semicircle is much larger than the high-frequency semicircle, implying that the low-frequency resistance $R_1 + R_2 + R_3$ is much higher than the high-frequency resistance R_1 and the intermediate-frequency resistance $R_1 + R_2$. In the case of the composite with the high volume fraction of CAM particles, the high-frequency semicircle is much larger than the low-frequency semicircle, implying that the intermediate-frequency resistance $R_1 + R_2$ and the low-frequency resistance $R_1 + R_2 + R_3$ exhibit very similar values.

From the resistances R_1, R_2, and R_3 obtained by fitting, we calculate the high-frequency conductivity σ_{hf}, the intermediate-frequency conductivity σ_{if} and the low-frequency conductivity σ_{lf} of the composite cathodes as follows

$$\sigma_{hf} = \frac{d}{A \cdot R_1} \tag{1}$$

$$\sigma_{if} = \frac{d}{A \cdot (R_1 + R_2)} \tag{2}$$

$$\sigma_{lf} = \frac{d}{A \cdot (R_1 + R_2 + R_3)} \tag{3}$$

In Figure 4, we plot the high-frequency conductivity σ_{hf} vs. the volume fraction of the CAM particles, ε_{CAM}, for all four active materials and for two pressures for each material. The data give strong indication for a linear relation between σ_{hf} and ε_{CAM} with a positive slope. In Figure 5, we plot the intermediate-frequency conductivity σ_{if} vs. the volume fraction of the CAM particles ε_{CAM}. In this plot, different type of relations $\sigma_{if}(\varepsilon_{CAM})$ are observable, i.e., relations with a positive slope, relations with a negative slope, and relations with a minimum around $\varepsilon_{CAM} = 0.5$. In Figure 6, we plot the low-frequency conductivity σ_{lf} vs. ε_{CAM} for all four active materials. In this plot, we observe a positive slope and a positive curvature of the data.

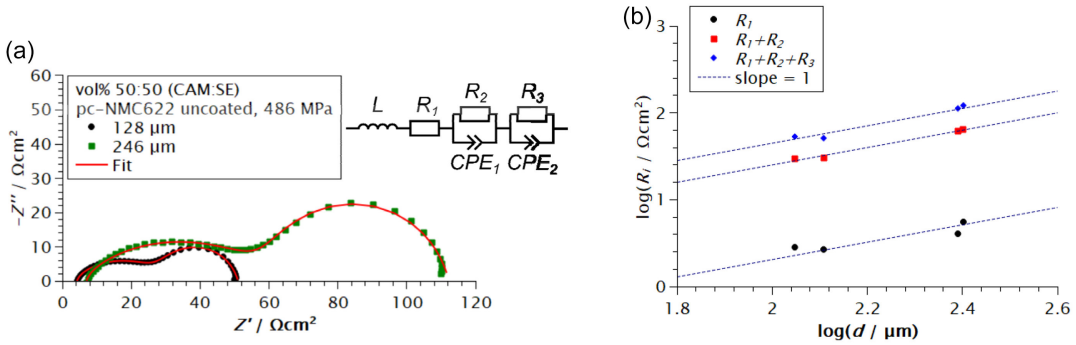

FIGURE 2 | (a) Nyquist impedance plot of two composite cathodes composed of 50 vol% uncoated pc-NMC622 particles and 50 vol% 0.67 Li_3PS_4 + 0.33 LiI particles at a pressure of 486 MPa. The cathode thickness is 128 and 246 µm, respectively. The inset shows the equivalent circuit used for fitting the spectra. (b) Resistances R_1, R_1+R_2, and $R_1+R_2+R_3$ plotted versus the cathode thickness (log–log plot).

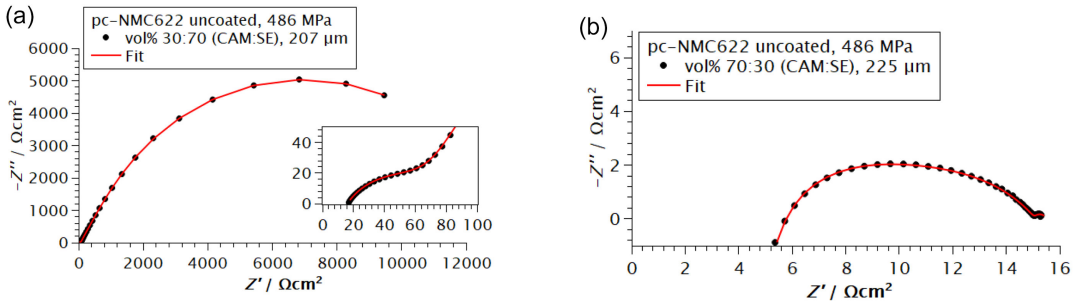

FIGURE 3 | Nyquist impedance plots of (a) a composite cathode composed of 30 vol% uncoated pc-NMC622 particles and 70 vol% 0.67 Li_3PS_4 + 0.33 LiI particles at a pressure of 486 MPa and of (b) a composite cathode composed of 70 vol% uncoated pc-NMC622 particles and 30 vol% 0.67 Li_3PS_4 + 0.33 LiI particles at a pressure of 486 MPa.

3.4 | Physical Interpretation of the Conductivities

Since the impedance measurements on the composites were carried out under ion-blocking conditions, the low-frequency conductivity σ_{lf} is identical to the electronic conductivity of the composite $\sigma_{eon}^{composite}$

$$\sigma_{lf} = \sigma_{eon}^{composite} = \frac{\sigma_{eon}^{CAM} \cdot \varepsilon_{CAM}}{\tau_{eon}} \tag{4}$$

Here, σ_{eon}^{CAM} and τ_{eon} denote the electronic conductivity of the pure CAM and the electronic tortuosity of the composite, respectively. τ_{eon} decreases with increasing volume fraction ε_{CAM}. Consequently, $\sigma_{eon}^{composite}$ increases with ε_{CAM} in a superlinear fashion (Figure 6), i.e., the $\sigma_{eon}^{composite}(\varepsilon_{CAM})$ data are characterized by a positive slope and a positive curvature, see also schematic illustration in Figure 7a.

At intermediate and high frequencies, more localized movements of the carriers determine the conductivity spectra, and the blocking of the ions by the metal electrodes is not relevant. Consequently, both types of charge carriers contribute to the conductivity. In classical work on the impedance spectra of mixed ionic-electronic conductors (MIECs), a "parallel conductivity" is discussed, which is the sum of the electronic and the ionic conductivity [20, 21]. In our case, this parallel conductivity $\sigma_{par}^{composite}$ can be defined as:

$$\sigma_{par}^{composite} = \sigma_{eon}^{composite} + \sigma_{ion}^{composite} = \frac{\sigma_{eon}^{CAM} \cdot \varepsilon_{CAM}}{\tau_{eon}} + \frac{\sigma_{ion}^{SE} \cdot (1 - \varepsilon_{CAM})}{\tau_{ion}} \tag{5}$$

Here, σ_{ion}^{SE} and τ_{ion} denote the ionic conductivity of the pure SE and the ion transport tortuosity in the composite, respectively.

In Figure 7 (a), we illustrate the influence of the CAM volume fraction ε_{CAM} on the electronic, ionic and parallel conductivity of the composite cathodes, $\sigma_{eon}^{composite}$, $\sigma_{ion}^{composite}$ and $\sigma_{par}^{composite}$, respectively. The $\sigma_{eon}^{composite}(\varepsilon_{CAM})$ curve is characterized by a positive slope and a positive curvature. Since the ion transport tortuosity τ_{ion} increases with increasing ε_{CAM}, the $\sigma_{ion}^{composite}(\varepsilon_{CAM})$ curve is characterized by a negative slope and a positive curvature. Consequently, the parallel conductivity $\sigma_{par}^{composite}(\varepsilon_{CAM})$ exhibits a positive slope in the case of $\sigma_{eon}^{composite} > \sigma_{ion}^{composite}$ and a negative slope in the case of $\sigma_{ion}^{composite} > \sigma_{eon}^{composite}$. Since both curves $\sigma_{eon}^{composite}(\varepsilon_{CAM})$ and $\sigma_{ion}^{composite}(\varepsilon_{CAM})$ exhibit a positive curvature, the $\sigma_{par}^{composite}(\varepsilon_{CAM})$ curve exhibits always a positive curvature, see Figure 7a.

Such features are exactly observable in the $\sigma_{if}(\varepsilon_{CAM})$ data shown in Figure 5. All data give indication for a positive curvature of $\sigma_{if}(\varepsilon_{CAM})$. This gives strong indication that the intermediate frequency conductivity can indeed by identified with the parallel conductivity, i.e., $\sigma_{if} = \sigma_{par}^{composite}$. Regarding the slope of $\sigma_{if}(\varepsilon_{CAM})$, we consider the following examples. (i) The data for uncoated sc- and pc-NMC622 at 98 MPa are dominated by the ionic conductivity at low ε_{CAM} values (negative slope) and by the electronic conductivity at high ε_{CAM} values (positive slope). Increasing the pressure to 486 MPa leads to a stronger increase of the electronic conductivity as compared to the ionic conductivity, and the electronic conductivity dominates for all

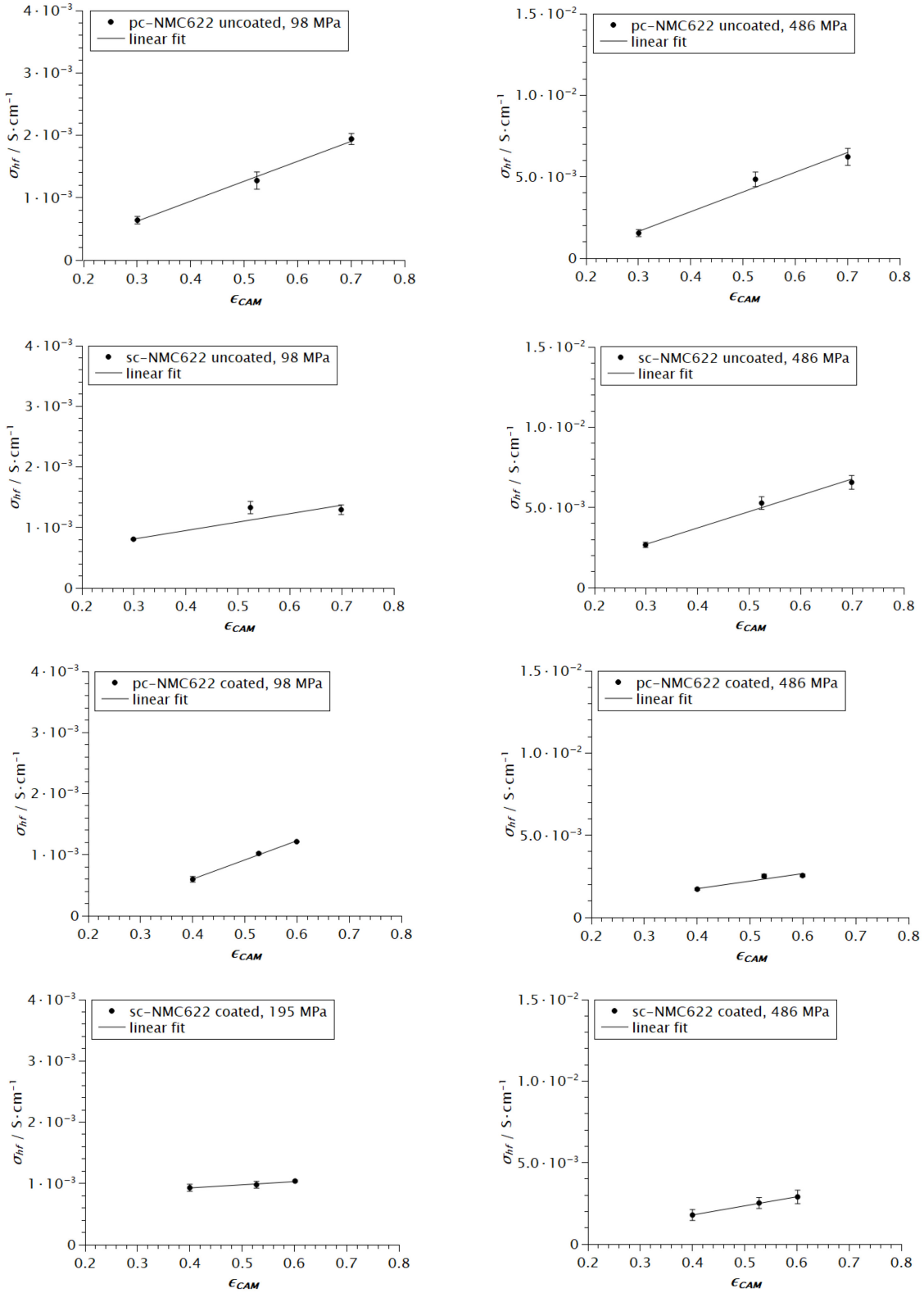

FIGURE 4 | High-frequency conductivity σ_{hf} plotted vs. the volume fraction of the CAM particles ε_{CAM} for four different active materials and at two different pressures for each material.

ε_{CAM} values (positive slope). (ii) The data for coated pc-NMC622 at 98 MPa are dominated by the ionic conductivity at 98 MPa and by the electronic conductivity at 486 MPa. This indicates that the coating lowers the electronic conductivity. (iii) The data for coated sc-NMC622 at both pressures are dominated by the ionic conductivity at low ε_{CAM} values (negative slope) and by the electronic conductivity at high ε_{CAM} values (positive slope). This gives indication that the electronic conductivity of sc-NMC622 is lowered more strongly by the coating than the electronic conductivity of pc-NMC622.

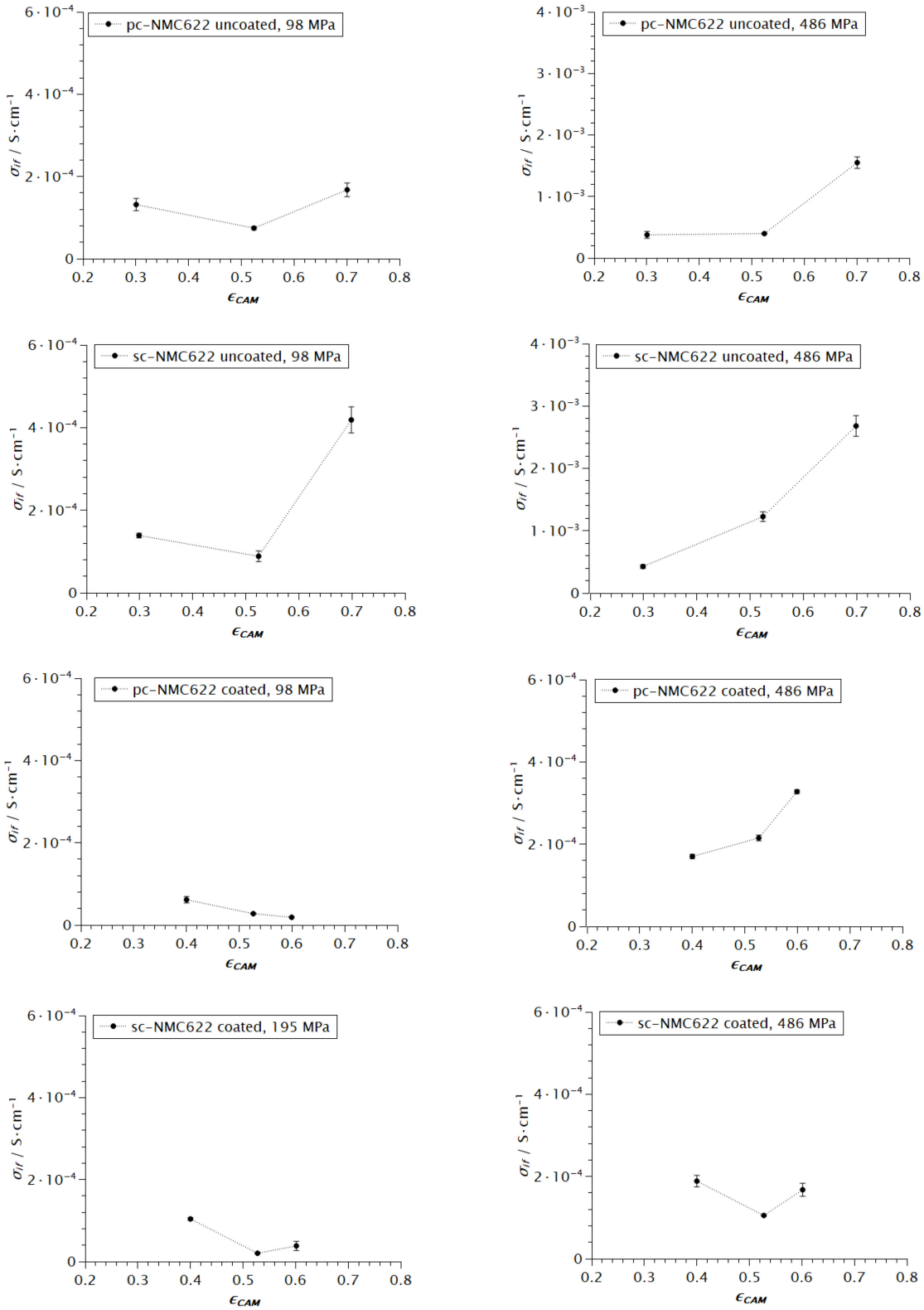

FIGURE 5 | Intermediate-frequency conductivity σ_{if} plotted vs. the volume fraction of the CAM particles ε_{CAM} for four different active materials and at two different pressures for each material.

Finally, we consider the high-frequency conductivity σ_{hf}. The linear relation between σ_{hf} and ε_{CAM} suggests that ionic and electronic tortuosities do not influence σ_{hf}. This is plausible, since at high frequencies, the charge carriers move over very short distances, so that the influence of geometrical tortuosities and constrictivities on the local movements should become negligible, see Figure 7b. Thus, σ_{hf} should be given by

$$\sigma_{hf} = \sigma_{eon}^{CAM} \cdot \varepsilon_{CAM} + \sigma_{ion}^{SE} \cdot (1 - \varepsilon_{CAM}) = \sigma_{ion}^{SE} + \left(\sigma_{eon}^{CAM} - \sigma_{ion}^{SE}\right) \cdot \varepsilon_{CAM} \quad (6)$$

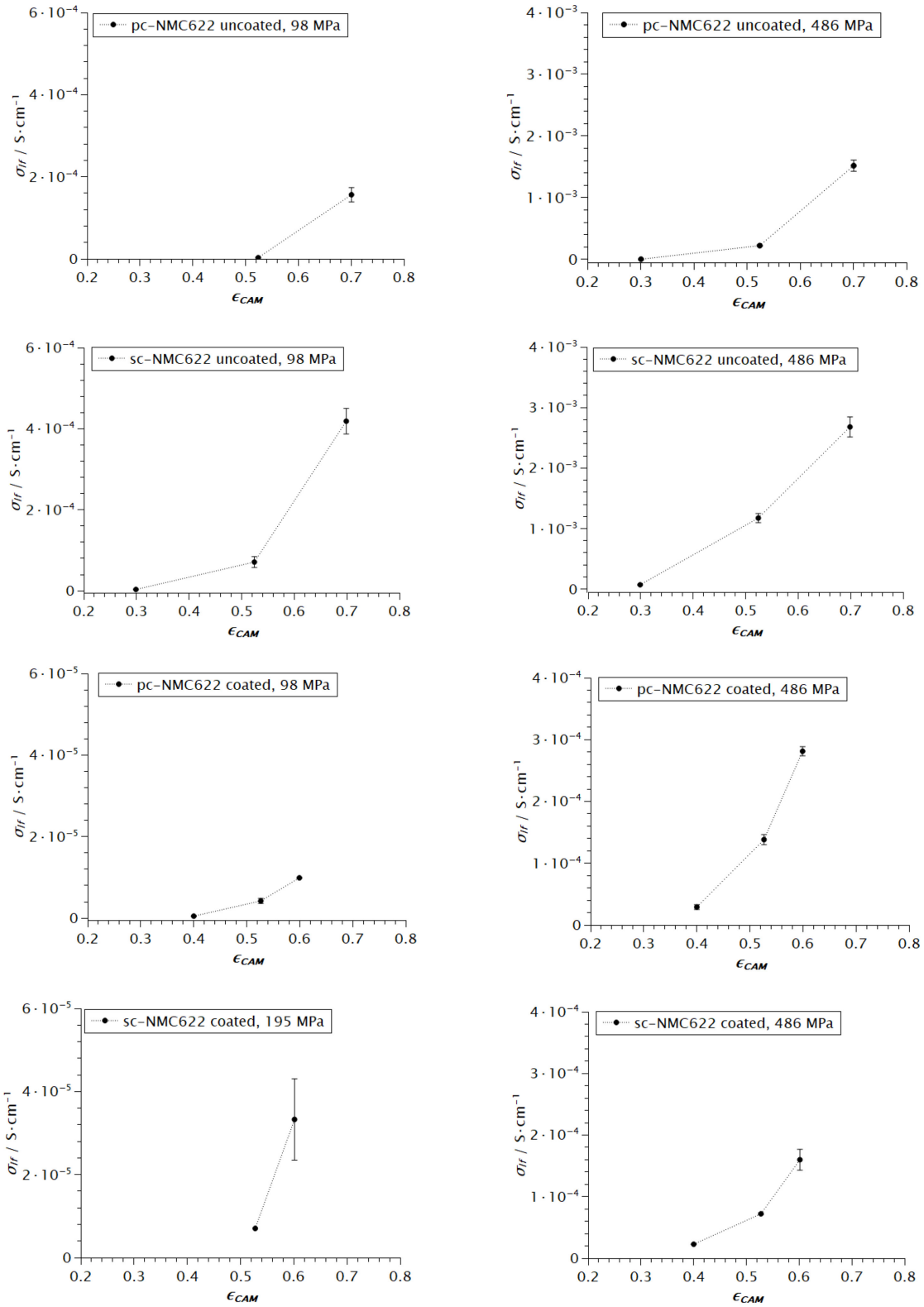

FIGURE 6 | Low-frequency conductivity σ_{lf} plotted vs. the volume fraction of the CAM particles ε_{CAM} for four different active materials and at two different pressures for each material. In two cases at low ε_{CAM}, σ_{lf} could not be determined, since the maximum of the low-frequency semicircle was located outside the frequency range of the impedance measurements.

The slope of $\sigma_{hf}(\varepsilon_{CAM})$ is given by the difference of the electronic conductivity of the CAM and the ionic conductivity of the SE, which is positive in most cases. Only in the case of coated sc-NMC622 at a pressure of 195 MPa, the slope is close to zero. The electronic conductivity of coated sc-NMC622 at a pressure of 195 MPa is around 0.96 mS cm^{-1} [22] and is indeed close to the ionic conductivity of 0.67 Li_3PS_4 + 0.33 LiI (0.73 mS cm^{-1}) at this pressure.

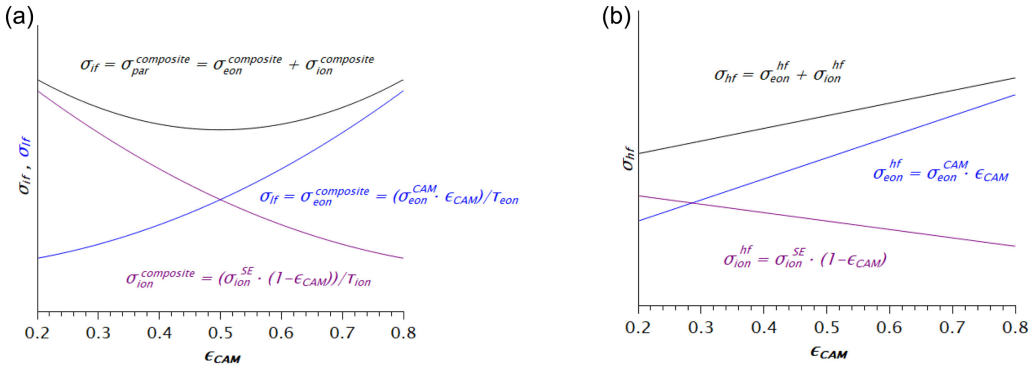

FIGURE 7 | Sketch illustrating the influence of the CAM volume fraction, ε_{CAM}, on the low-frequency conductivity $\sigma_{lf} = \sigma_{eon}^{composite}$, intermediate-frequency conductivity $\sigma_{if} = \sigma_{par}^{composite}$, and high-frequency conductivity σ_{hf} of CAM/SE composites.

3.5 | Influence of Active Material Morphology and Coating on Composite Microstructure and Tortuosities

Equation (4) was used to calculate the electronic tortuosity τ_{eon}, and subsequently Equation (5) was used to calculate the ion transport tortuosity τ_{ion}.

As seen from Figure 8a, the electronic tortuosity τ_{eon} is strongly influenced by the pressure as well as by the morphology of the CAM particles and the particle coating. Increasing the pressure from 44 MPa to 663 MPa at $\varepsilon_{CAM} = 0.5$ leads typically to a drop of τ_{eon} by one order of magnitude. Remarkably, the $LiNbO_3$ coating leads to an increase of the electronic tortuosity in the case of sc-NMC622 and to a drop of the electronic tortuosity in the case of pc-NMC622. In order to elucidate the origin of these findings, we have taken SEM images of the pure NMC622 particles (Figure 9), SEM/EDX images of the CAM/SE composite powder after mixing in a mortar (Figure 10), and cross-sectional SEM/EDX images of the composite pellets after a FIB cut (Figure 11). The SEM images of the pure uncoated sc-NMC622 particles in Figure 9 show that these particles exhibit a high tendency for agglomeration, while the $LiNbO_3$-coated sc-NMC622 particles exhibit a lower tendency. The same trend is also observable in the SEM images of the CAM/SE composite powder after mixing in a mortar, see Ni EDX mapping in Figure 10. This indicates that the agglomeration of uncoated sc-NMC622 particles in the composite and the resulting good electronic contacts lead to a low electronic tortuosity. Due to the smaller degree of agglomeration of the coated sc-NMC622 particles, the electronic tortuosity of the coated sc-NMC622-based composite is higher. In contrast, the SEM images of pure pc-NMC622 particles point to a low tendency for agglomeration, independent of a $LiNbO_3$ coating. Figure 8a shows that the electronic tortuosity of the coated pc-NMC622-based composite is lower than that of the uncoated pc-NMC622-based composite. This seems to be a paradox observation at first sight, which can, however, be explained as follows. The electronic conductivity of pure coated pc-NMC622 particles is much lower than the electronic conductivity of pure uncoated pc-NMC622 particles, most likely due to the insulating nature of the coating. However, the CAM/SE composite preparation in the mortar leads to a cracking of uncoated particles and to a rather homogeneous coating of most particles by the solid electrolyte, see SEM image of the composite powder in Figure 10, schematic illustration in Figure 12, and cross-sectional SEM images of the composite pellet in Figure 11. This SE coating of the previously uncoated particles together with the cracking of pc-NMC622 particles diminishes the electronic transport strongly, implying a high electronic tortuosity. The mixing of the $LiNbO_3$-coated pc-NMC622 particles with the SE particles in the mortar leads also to a cracking of the pc-NMC622 particles, but the pc-NMC622 particles are only partially coated by the solid electrolyte; see SEM image in Figure 10 and schematic illustration in Figure 12. Therefore, the electronic transport is only weakly diminished by the composite preparation, implying a rather low electronic tortuosity.

In Figure 8b, the ionic tortuosities τ_{ion} of the composite electrodes at $\varepsilon_{CAM}=0.5$ are plotted versus pressure. The pressure dependence of τ_{ion} is weak suggesting that the compaction of the solid

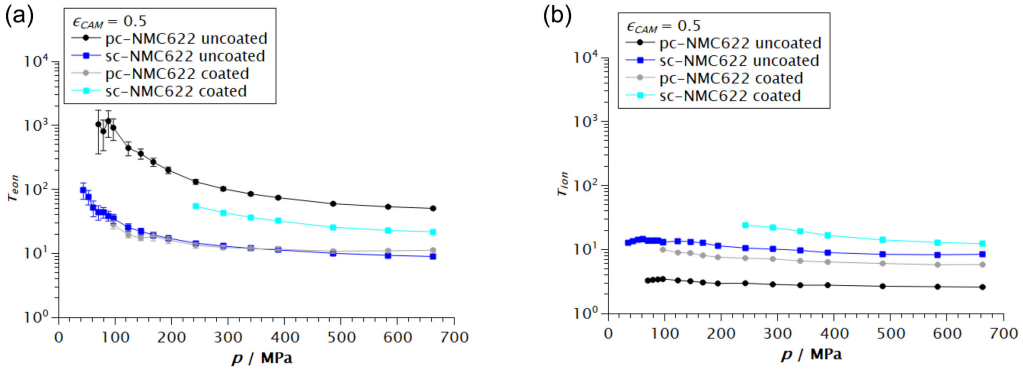

FIGURE 8 | (a) Electronic tortuosity τ_{eon} and (b) ionic tortuosity τ_{ion} of composite cathodes with $\varepsilon_{CAM}=0.5$.

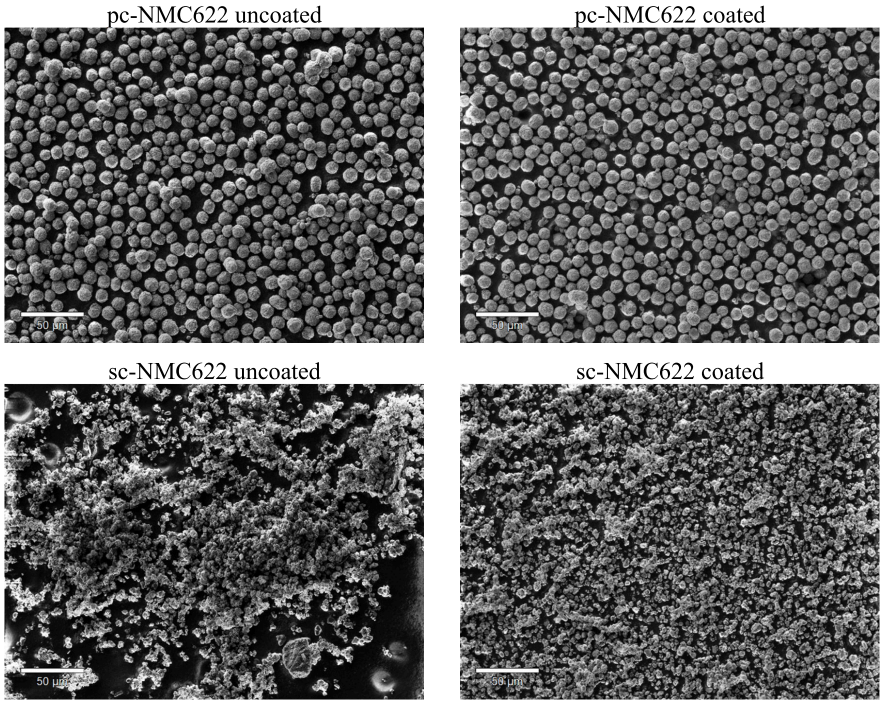

FIGURE 9 | SEM images of pure uncoated and coated pc- and sc-NMC622 particles.

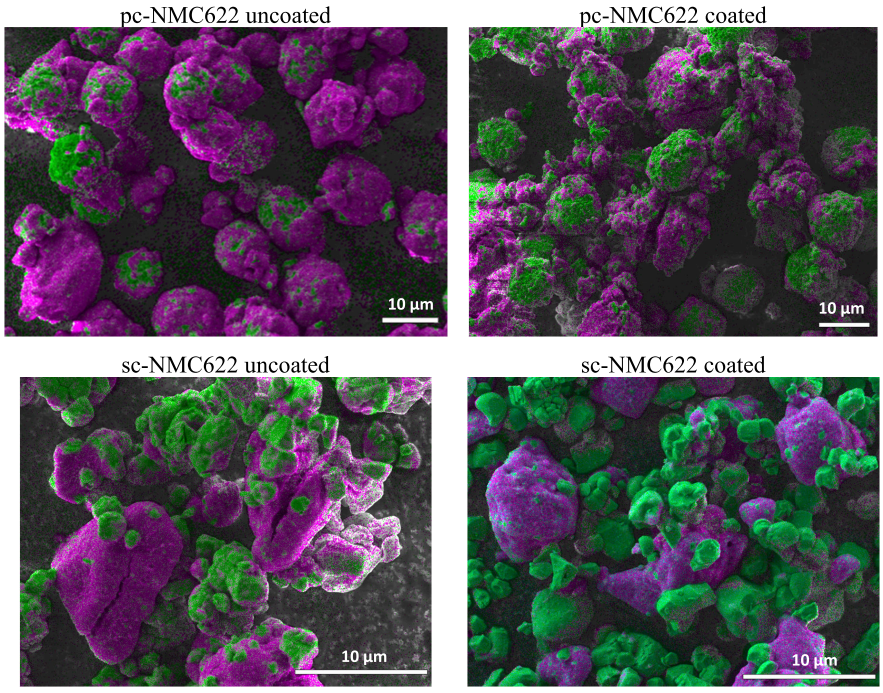

FIGURE 10 | SEM images of CAM/SE powders after mixing the particles in a mortar (purple: S EDX intensity mapping; green: Ni EDX intensity mapping).

electrolyte in the composite pellets with increasing pressure is similar to the compaction in the pure solid electrolyte pellets. The pc-NMC622-based composite cathodes exhibit lower τ_{ion} values than the sc-NMC622-based composite cathodes. Most likely, the SE coating of the pc-NMC622 particles (see Figures 10 and 12) during composite preparation facilitates ion transport in the composite, implying a low ion transport tortuosity. In this context, it is worth mentioning that the idea of coating active material particles with SE by means of a solution-based method in order to reduce the ion transport resistances has been demonstrated in the literature [23]. However, this method leads to a reduced ionic conductivity of the SE, while this is not the case for our "dry coating" of pc-NMC622 particles during mixing with SE particles in a mortar. The SEM images of the sc-NMC622-based composite powders in Figure 10 show that the sc-NMC622 particles are *not* coated by the SE, but the SE exists primarily as large particles

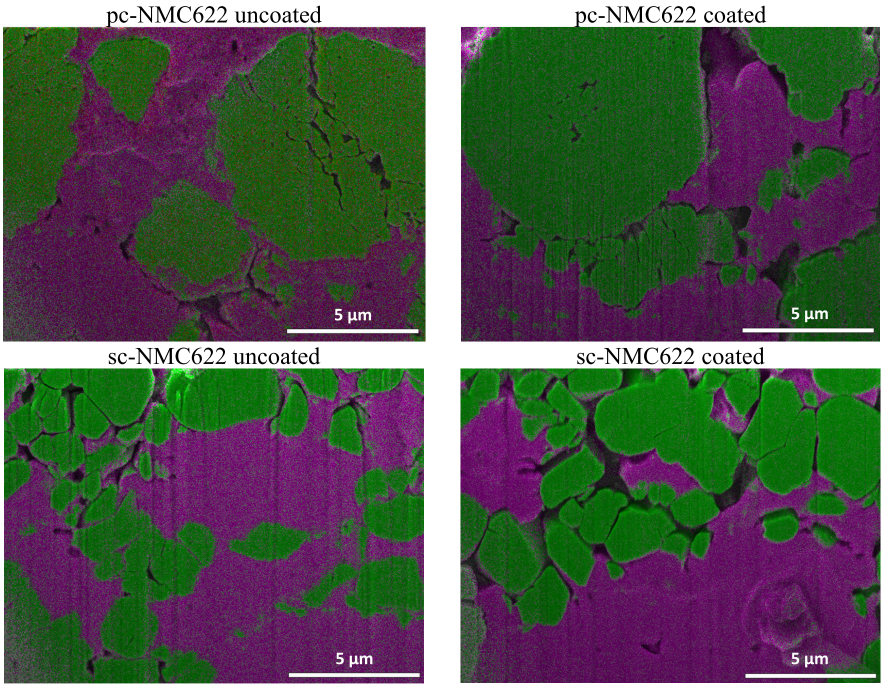

FIGURE 11 | SEM images of cross sections of composite pellets after applying a pressure of 663 MPa (purple: S EDX intensity mapping; green: Ni EDX intensity mapping).

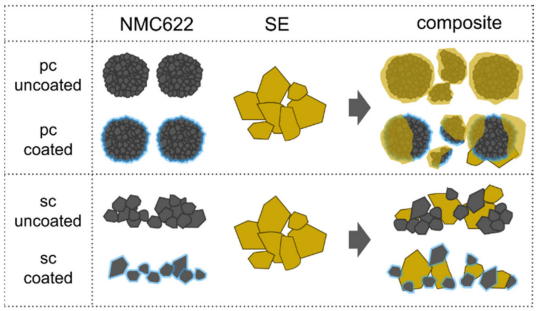

FIGURE 12 | Schematic illustration of the influence of NMC622 particle morphology and coating on the microstructure of the composite powder prepared in a mortar.

between the sc-NMC622 particles. Thus, the ion transport between the large SE particles should be impeded by the sc-NMC622 particles, leading to a high ion transport tortuosity.

4 | Conclusions

The impedance spectra of CAM/SE composites yield three different conductivities, a high-frequency conductivity σ_{hf}, an intermediate-frequency conductivity σ_{if}, and a low-frequency conductivity σ_{lf}. Since our measurements are carried out under ion-blocking conditions, the low-frequency conductivity σ_{lf} can be identified with the electronic conductivity of the composite, while the intermediate-frequency conductivity σ_{if} can be identified with the parallel conductivity (sum of electronic and ionic conductivity) of the composite. The physical meaning of the high-frequency conductivity σ_{hf} is rarely discussed in the literature. Our analysis of the influence of the volume fraction of CAM particles and SE particle on σ_{hf} gives strong indication that σ_{hf} can be identified with a parallel conductivity being governed by highly local movements of ions and electrons without tortuosity effects.

Electronic and ionic tortuosities can be obtained from the values of σ_{lf} and σ_{if}, except in cases with $\sigma_{lf} \approx \sigma_{if}$. We find that the morphology and coating of the CAM particles exert a strong influence on the microstructure of the CAM/SE composites and thus on the electronic and ionic tortuosities. Sc-NMC622 particles form aggregates, which do not interact strongly with the solid electrolyte particles during the preparation of the composite in a mortar. Consequently, the composites contain aggregated sc-NMC622 particles and large SE particles in between. The aggregation of the sc-NMC622 particles leads to rather fast electronic transport (low electronic tortuosity), while the existence of large SE particles results in rather slow ionic transport (high ionic tortuosity). In contrast, pc-NMC622 particles exhibit a low tendency for agglomeration and interact strongly with the SE during the preparation of the composite. This leads to homogeneous SE coating layers on the uncoated pc-NMC622 particles, resulting in rather fast ionic transport (low ionic tortuosity) and rather slow electronic transport (high electronic tortuosities). $LiNbO_3$-coated pc-NMC622 particles are also coated by SE during mixing, however the coating is less homogeneous. This leads to higher ionic tortuosities than obtained for uncoated pc-NMC622/SE composites.

The difference between sc-NMC622 and pc-NMC622 regarding NMC–NMC agglomeration and NMC–SE interaction is most likely related to the surface properties of the NMC particles, e.g., to different surface chemistries or to different degrees of crystallinity at the surface. Consequently, future studies on the NMC particle surfaces (transmission electron microscopy, XPS) are essential for achieving a better understanding of the relation between surface chemistry and particle–particle interactions in composite cathodes.

Finally, we note that in future studies, processes taking place during release of the fabrication pressure and during the application of an operational stack pressure to composite cathodes should be characterized in more detail. These processes are expected to be more reversible in nature and should exert a strong influence on the power density of practical ASSBs. The results of such studies together with the results of the present study should yield important input parameters for ASSBs cell performance simulations, which are essential to deconvolute the influence of various factors on the cell performance.

Acknowledgments

Open Access funding enabled and organized by Projekt DEAL.

Funding

This research was supported by the Deutsche Forschungsgemeinschaft (DFG) in the framework of the projects RO 1213/20-1 and RO 1213/14-2.

Conflicts of Interest

The authors declare no conflicts of interest.

Data Availability Statement

Data supporting the findings of this study are shown in the Supporting Information. Further data are available from the corresponding author upon reasonable request.

References

1. J. Janek and W. G. Zeier, "A Solid Future for Battery Development," *Nature Energy* 1 (2016): 16141.

2. J. Amici, P. Asinari, E. Ayerbe, et al., "A Roadmap for Transforming Research to Invent the Batteries of the Future Designed Within the European Large Scale Research Initiative BATTERY 2030+," *Advanced Energy Materials* 12 (2022): 2102785.

3. H. Q. Pham, H.-Y. Lee, E.-H. Hwang, Y.-G. Kwon, and S.-W. Song, "Non-Flammable Organic Liquid Electrolyte for High-Safety and High-Energy Density Li-Ion Batteries," *Journal of Power Sources* 404 (2018): 13–19.

4. F. Gebert, M. Longhini, F. Conti, and A. J. Naylor, "An Electrochemical Evaluation of State-of-the-Art Non-Flammable Liquid Electrolytes for High-Voltage Lithium-Ion Batteries," *Journal of Power Sources* 556 (2023): 232412.

5. A. M. Abakumov, S. S. Fedotov, E. V. Antipov, and J.-M. Tarascon, "Solid State Chemistry for Developing Better Metal-Ion Batteries," *Nature Communications* 11 (2020): 4976.

6. S. Randau, D. A. Weber, O. Kötz, et al., "Benchmarking the Performance of All-Solid-State Lithium Batteries," *Nature Energy* 5 (2020): 259–270.

7. C. Wang, J. Liang, Y. Zhao, M. Zheng, X. Li, and X. Sun, "All-Solid-State Lithium Batteries Enabled by Sulfide Electrolytes: From Fundamental Research to Practical Engineering Design," *Energy & Environmental Science* 14 (2021): 2577–2619.

8. P. Minnmann, F. Strauss, A. Bielefeld, et al., "Designing Cathodes and Cathode Active Materials for Solid-State Batteries," *Advanced Energy Materials* 12 (2022): 2201425.

9. Z. Wu, X. Li, C. Zheng, et al., "Interfaces in Sulfide Solid Electrolyt-Based All-Solid-State Lithium Batteries: Characterization, Mechanisms and Strategy," *Electrochemical Energy Reviews* 6 (2023): 10.

10. J. Kim, M. Eom, S. Noh, and D. Shin, "Effect of Mixing Method on the Properties of Composite Cathodes for All-Solid-State Lithium Batteries Using Li_2S–P_2S_5 Solid Electrolytes," *Journal of Power Sources* 244 (2013): 476–481.

11. B. Tjaden, D. J. L. Brett, and P. R. Shearing, "Tortuosity in Electrochemical Devices: A Review of Calculation Approaches," *International Materials Reviews* 63 (2018): 47–67.

12. C. König, V. Miß, L. Janin, and B. Roling, "Mitigating the Ion Transport Tortuosity in Composite Cathodes of All-Solid-State Batteries by Wet Milling of the Solid Electrolyte Particles," *ACS Applied Energy Materials* 6 (2023): 9356–9362.

13. P. Minnmann, L. Quillman, S. Burkhardt, F. H. Richter, and J. Janek, "Editors' Choice—Quantifying the Impact of Charge Transport Bottlenecks in Composite Cathodes of All-Solid-State Batteries," *Journal of the Electrochemical Society* 168 (2021): 040537.

14. M. Kroll, M. Duchardt, S. L. Karstens, et al., "Sheet-Type All-Solid-State Batteries with Sulfidic Electrolytes: Analysis of Kinetic Limitations Based on a Cathode Morphology Study," *Journal of Power Sources* 505 (2021): 230064.

15. T. Shi, Q. Tu, Y. Tian, et al., "High Active Material Loading in All-Solid-State Battery Electrode via Particle Size Optimization," *Advanced Energy Materials* 10 (2020): 1902881.

16. S.-Y. Park, J. Jeong, and H.-C. Shin, "Geometrical Effect of Active Material on Electrode Tortuosity in All-Solid-State Lithium Battery," *Applied Sciences* 12 (2022): 12692.

17. M. So, G. Inoue, R. Hirate, K. Nunoshita, S. Ishikawa, and Y. Tsuge, "Effect of Mold Pressure on Compaction and Ion Conductivity of All-Solid-State Batteries Revealed by the Discrete Element Method," *Journal of Power Sources* 508 (2021): 230344.

18. V. Mereacre, P. Stüble, A. Ghamlouche, and J. R. Binder, "Enhancing the Stability of $LiNi_{0.5}Mn_{1.5}O_4$ by Coating with $LiNbO_3$ Solid-State Electrolyte: Novel Chemically Activated Coating Process versus Sol-Gel Method," *Nanomaterials* 11 (2021): 548.

19. J. Haust, Y. Guo, J. Belz, et al., "$LiNbO_3$ Coatings on NCM622: Structure and Performance Insights," *Advanced Materials Interfaces* 12 (2025): e00590.

20. J. Jamnik and J. Maier, "Treatment of the Impedance of Mixed Conductors Equivalent Circuit Model and Explicit Approximate Solutions," *Journal of the Electrochemical Society* 146 (1999): 4183–4188.

21. J. Jamnik, J. Maier, and S. Pejovnik, "A Powerful Electrical Network Model for the Impedance of Mixed Conductors," *Electrochimica Acta* 44 (1999): 4139–4145.

22. V. Miß, S. Seus, A. Marx, et al., "Influence of Pressure, Particle Morphology, Coating, and Heat Treatment on the Effective Electronic Conductivity of Cathode Active Materials for All-Solid-State Batteries," *ACS Materials Letters* 7 (2025): 2262–2269.

23. K. H. Park, D. Y. Oh, Y. E. Choi, et al., "Solution-Processable Glass LiI-Li_4SnS_4 Superionic Conductors for All-Solid-State Li-Ion Batteries," *Advanced Materials* 28 (2016): 1874–1883.

Supporting Information

Additional supporting information can be found online in the Supporting Information section. Powder XRD pattern of the amorphous solid electrolyte; Pressure protocol of impedance measurements; Thickness dependence of resistances; SEM images of pure uncoated and coated NMC622 particles.